# Excellent surface plasmon and hot carrier properties of transition metal nitride at different temperatures

Chaochao Jian, Xiangchao Ma [ORCID],[*] Xin Wu, Jianqi Zhang, and Jiali Jiang

*School of Optoelectronic Engineering, Xidian University, Xi'an, 710071, China*

Plasmonic materials that exhibit excellent plasmonic behavior at high temperatures would greatly expand existing applications, but the search for such materials is ongoing. Transition metal nitrides with good conductivity and high-temperature stability are promising candidates for temperature-dependent plasmonic applications. Here, we systematically investigate the temperature-dependent surface plasmon and hot carrier properties of TiN and VN. Significantly, high temperatures significantly affect the phonon-assisted intraband transition processes. Meanwhile, TiN and VN exhibit efficient optical absorption and low surface plasmon loss at different temperatures, which are comparable to or even higher than Ag. In particular, the surface plasmon response of TiN extends to visible light, making it an excellent candidate for low-loss and broadband plasmonic applications at high temperatures. In contrast, VN exhibits a much narrower plasmonic window, which is mainly suitable for infrared low-loss plasmonic devices. For hot carriers, the energy and probability distributions of hot holes in TiN and hot electrons in VN exhibit robustness to temperature. Meanwhile, transport properties indicate that the temperature effect on hot holes is significantly higher than that on hot electrons in TiN and VN. Therefore, we expect that the reported results will provide theoretical guidance for the design of next-generation high-temperature plasmonic devices.

## I. INTRODUCTION

Surface plasmons of metallic materials hold the exciting promise of shrinking optical and photonic devices from the micro- to nanoscale [1,2], and their nonradiative decay generating hot carriers hold promise for improving optoelectronic conversion efficiency [3,4]. Conventional noble metals (Au, Ag) have long been considered excellent plasmonic materials [5], which provide fundamental solutions for the above-mentioned applications. However, the low-melting noble metals do not meet the application-specific requirements in high-temperature environments, such as aerospace and power engineering.

Recently, transition metal nitrides [6–8] with good metallic and high-temperature stable properties exhibit good plasmonic properties as alternative "noble metals," which have great potential for high-temperature plasmonic applications. For example, W. Wang *et al.* experimentally demonstrated that VN films with superior thermal stability at 800 °C may potentially be used for efficient solar absorption [9]. X. Wang *et al.* presented a hybrid plasmonic Au-TiN vertically aligned nanocomposite to attain optical flexibility including change of surface plasmon resonances in the UV-visible range [10]. In general, the plasmon properties are closely related to the carrier concentration*s*, phonon properties, and carrier energy distribution in metallic materials. The electric field and impurity doping are important means to adjust the carrier concentrations. For example, Hu *et al.* experimentally

demonstrated electric field modulation produces high-concentration hole-doped graphene, resulting in broadly tunable graphene plasmons [11]. Moreover, Shirodkar *et al.* indicated that the high-concentration doping of lithium in graphene shifts the plasmon frequen*cy* into the visible range [12]. Meanwhile, impurity doping also increases the phase space for electron-phonon scattering, resulting in an increase in plasmon decay. Notably, the temperature has richer effects on surface plasmon properties, including temperature-dependent carrier density, scattering effects, and carrier distribution. For example, Kim *et al.* observed that the intensities of the plasmon resonance peaks increase significantly as the temperature drops, resulting from temperature-induced hole doping and the suppression of scattering [13]. Furthermore, Garcia *et al.* indicated that the temperature dependence of surface plasmon in NbAs is very strong at low frequencies [14], which is mainly caused by the temperature-dependent distribution of electrons and phonons. Therefore, for intrinsic transition metal nitrides, more studies on the temperature-dependent surface plasmon properties are urgently needed for the practical design of nanophotonic devices. In practice, the construction of high-temperature experimental environments in the laboratory is costly to implement and poorly reproducible. Therefore, it is necessary to find a theoretical tool with enough accuracy and independence of empirical parameters to fully evaluate temperature dependence of surface plasmon properties of transition metal nitrides, which can provide reliable theoretical guidance and thereby save a great deal of laboratory trial and error time. For example, the works of Gumbs *et al.* are a theoretical study of the temperature dependence of surface plasmon in graphene by the

---

[*]xcma@xidian.edu.cn

2D random-phase approximation (RPA) ring diagram polarization function at arbitrary temperatures [15,16]. Meanwhile, Iurov *et al.* theoretically investigated the plasmon dispersion and damping in the Dirac-cone materials and the $\alpha - \tau_3$ model of 2D nanostructures based on the temperature-dependent polarization function [17–20]. However, the current theoretical studies still have little knowledge about the temperature dependence of surface plasmon properties in transition metal nitrides at the microscopic level.

Theoretically, surface plasmon inevitably decays rapidly into electron-hole pairs in metallic materials. This plasmonic loss mechanism generates efficient hot carriers, which is of great significance for hot carrier-based applications such as photochemistry and photodetection [21–23]. Effective hot carrier devices require that the high-energy hot carrier in metallic materials remain a sufficiently long lifetime and transport distance at different temperatures. However, the current understanding of the temperature dependence of hot carrier properties is still lacking, which greatly hinders the determination of the true potential of these materials for hot carrier applications in high-temperature environments. Fundamentally, impurity, electron-electron, and electron-phonon scattering effects inevitably affect the carrier transport properties. For the hot carrier system at different temperatures, the numerical calculations by Patel *et al.* indicated that the impurity scattering rate shows little temperature dependence [24]. In addition, the concentration of unintentionally introduced impurities in pure transition metal nitrides studied here is generally low. Therefore, the study of temperature-dependent carrier transport properties ignores the impurity scattering effect*s*. In contrast, electron-electron and electron-phonon scattering generally exhibit strong temperature dependence. For example, Efetov *et al.* reported that the measured resistivity of graphene increases linearly with temperature [25]. Therefore, we systematically study the electron-electron and electron-phonon scattering effects on the hot carrier transport properties at different temperatures.

Here, based on the first-principles calculations without any empirical parameters, we comprehensively investigate the temperature dependence of the surface plasmon and hot carrier properties in two transition metal nitrides: TiN and VN [26,27]. Firstly, we calculate the temperature-dependent optical response dielectric function, which includes the main losses based on Drude resistance, direct interband-, and phonon-assisted intraband electronic transitions processes. The results show that the temperature significantly affects the phonon-assisted intraband electronic transitions at low energies. Meanwhile, our calculated complex dielectric functions of VN and TiN are consistent with the results at room temperature in reference [27], indicating the reliability of our theoretical calculation. With these accurate results, we study the temperature-dependent surface plasmon properties, including two figures of merit in typical plasmonic applications. The results show that the low-loss surface plasmon polaritons in TiN extend into the visible range at different temperatures, making it an excellent noble-metal alternative for high-temperature plasmonic applications. In addition, we study the temperature dependence of hot carrier properties in TiN and VN, including temperature-dependent energy distribution, carrier lifetime, and mean-free path, which provides deeper insight toward the relationship between hot carrier transport properties and temperature at the microscopic level.

## II. COMPUTATIONAL METHODS

We first calculate the electronic structure, phonon spectrum, and electron-phonon matrix elements of TiN and VN from first principles using density-functional theory (DFT) as implemented by the open-source code JDFTX software [28]. We use the Perdew-Burke-Ernzerhof generalized-gradient approximation [29] to the exchange-correlation functional and norm-conserving SG15 pseudopotentials [30]. For TiN and VN, we use a kinetic energy cutoff of 25 hartrees and Fermi-Dirac smearing of 0.01 hartree. To obtain well-converged results, we use a dense $14 \times 14 \times 14$ $k$-point mesh for TiN and $8 \times 8 \times 8$ $k$-point mesh for VN, respectively. We use a $4 \times 4 \times 4$ supercell for TiN and VN, respectively, to calculate the phonon states.

Next, we construct the maximally localized Wannier functions (MLWFs) [31,32] to exactly reproduce the DFT band structures up to at least 30 eV from the Fermi level. Specifically, we use 23 Wannier bands for TiN and 34 Wannier bands for VN, respectively, to reproduce the orbital energies, phonon energies, and electron-phonon matrix elements at arbitrary wave vectors **k** for subsequent surface plasmon and hot carrier properties calculations.

### A. Dielectric function of the material

In general, the frequency-dependent complex conductivity $\sigma(\omega)$ is used to describe the optical and plasmonic responses of metallic materials, of which the real part can be written as [33,34]

$$\text{Re}\,\sigma(\omega) = \frac{\sigma_0 \tau_{D0}^{-1} \tau_D^{-1}(\omega)}{\left[\tau_D^{-1}(\omega)\right]^2 + \omega^2} + \text{Re}\,\sigma_{\text{inter}}(\omega). \tag{1}$$

In the first term, $\sigma_0 \tau_{D0}^{-1}$ represents the Drude resistance effects with $\sigma_0$ being DC conductivity and $\tau_{D0}$ being Drude momentum-relaxation time, which is calculated by

$$\frac{\sigma_0}{\tau_{D0}} = \int_{BZ} \frac{e^2 g_s d\mathbf{k}}{(2\pi)^d} \sum_n \delta(\varepsilon_{\mathbf{k}n} - \varepsilon_F)(v_{\mathbf{k}n} \otimes v_{\mathbf{k}n}), \tag{2}$$

where $\varepsilon_{\mathbf{k}n}$ is the Kohn-Sham energy of the electronic state with wave vector **k** and band index $n$, and $\varepsilon_F$ is the Fermi energy; $v_{\mathbf{k}n}$ is the band velocity with wave vector **k** and band index $n$; $g_s = 2$ is the spin-degeneracy factor, and $d$ is the dimension, which is 3 for bulk materials. Furthermore, $\tau_D^{-1}(\omega)$ is the frequency-dependent momentum relaxation rates, which encapsulate the phonon-assisted intraband electronic transition contributions to the optical and plasmonic response. From the Eliashberg spectral function [35,36], we calculate the frequency-dependent momentum relaxation rates $\tau_D^{-1}(\omega)$ as follows:

$$\tau_D^{-1}(\omega) = \frac{2\pi}{\hbar g(\varepsilon_F) b_T(\hbar\omega)} \sum_\alpha \int_{BZ} \frac{d\mathbf{q}}{(2\pi)^d} G_{\mathbf{q}\alpha}^p b_T(\hbar\omega - \hbar\omega_{\mathbf{q}\alpha}),$$
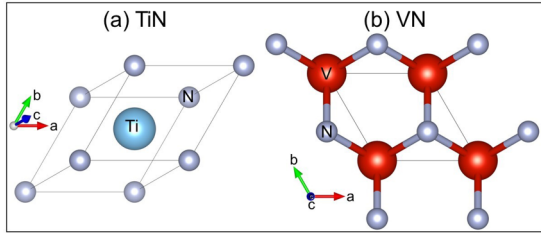$$\tag{3}$$

FIG. 1. Primitive unit cells of TiN (a) and VN (b).

where $b_T(\varepsilon) \equiv \frac{\varepsilon}{1-e^{-(\varepsilon/k_B T)}}$ and the dimensionless $G_{\mathbf{q}\alpha}^p$ is defined as

$$
G_{\mathbf{q}\alpha}^p \equiv \sum_{nn'} \int_{BZ} \frac{g_s \Omega dk}{(2\pi)^d} |g_{(\mathbf{k}+\mathbf{q})n',\mathbf{k}n}^{\mathbf{q}\alpha}|^2 \left( 1 - \frac{v_{\mathbf{k}n} \cdot v_{(\mathbf{k}+\mathbf{q})n'}}{|v_{\mathbf{k}n}||v_{(\mathbf{k}+\mathbf{q})_{n'}}|} \right)
$$
$$
\times \delta(\varepsilon_{\mathbf{k}n} - \varepsilon_F) \delta(\varepsilon_{(\mathbf{k}+\mathbf{q})n'} - \varepsilon_F),
$$

where $g(\varepsilon_F)$ is the density of electronic states near the Fermi energy, and $\hbar\omega_{\mathbf{q}\alpha}$ is the energy of phonon state with wave vector $\mathbf{q}$ and polarization index $\alpha$; $g_{(\mathbf{k}+\mathbf{q})n',\mathbf{k}n}^{\mathbf{q}\alpha}$ is the electron-phonon matrix element with electronic states labeled by wave vector $\mathbf{k}$, $\mathbf{q}$ and band index $n$, $n'$, and $\Omega$ is the unit-cell volume; $k_B$ is Boltzmann constant, and $T$ represents the temperature. We use $2 \times 10^7$ pairs $(\mathbf{k}, \mathbf{q})$ in the Brillouin zone to ensure convergence of the integrals in Eq. (3), and the temperature dependence of Eq. (3) is reflected in the parameter $k_B T$.

In the second term, $\text{Re}\sigma_{\text{inter}}(\omega)$ is the contribution due to direct interband electronic transitions. Using Fermi's golden rule for the real part, which is related to the imaginary part of corresponding $\varepsilon(\omega)$ [37,38] and is calculated by

$$
\text{Re}\sigma_{\text{inter}}(\omega) = \varepsilon_0\omega\left(\frac{\pi e^2}{\omega^2} \int_{BZ} \frac{g_s d\mathbf{k}}{(2\pi)^d} \sum_{nn'} (f_{\mathbf{k}n} - f_{\mathbf{k}n'})\right.
$$
$$
\left. \times \delta(\varepsilon_{\mathbf{k}n'} - \varepsilon_{\mathbf{k}n} - \hbar\omega)(v_{\mathbf{k}nn'}^* \otimes v_{\mathbf{k}nn'}) \right), \quad (4)
$$

where $\varepsilon_0$ is the vacuum dielectric constant, and $v_{\mathbf{k}nn'}$ is the matrix element of the velocity operator; $f_{\mathbf{k}n} = f(\varepsilon_{\mathbf{k}n}, T_e)$ is Fermi occupation of the electron state with wave vector $\mathbf{k}$ and band index $n$, in which the temperature dependence of Eq. (4) is embedded [14]. For the Brillouin-zone integral calculation in Eq. (4), we use a dense Monte Carlo sampling with $1.6 \times 10^7$ $\mathbf{k}$ to ensure convergence of the results.

Therefore, the imaginary part of the dielectric function, which is closely related to the conductivity of metallic ma-

terials, is calculated by

$$
\text{Im}\varepsilon(\omega) = \frac{\text{Re}\sigma(\omega)}{\varepsilon_0\omega}, \quad (5)
$$

where $\text{Re}\sigma(\omega)$ is the real part of the frequency-dependent complex conductivity, which is calculated by Eq. (1), and the corresponding real part of the dielectric function $\text{Re}\varepsilon(\omega)$ is obtained from the Kramers-Kronig relation [39].

According to the classical electrodynamic theory, polarizability $\chi(\omega)$ is defined as $\varepsilon(\omega) = 1 + \chi(\omega)$. Meanwhile, the dielectric function is calculated by $\varepsilon(\omega) = 1 + \frac{i\sigma(\omega)}{\varepsilon_0\omega}$. Therefore, the analytical expressions for the polarizability $\chi(\omega)$ can be expressed as

$$
\chi(\omega) = \frac{i}{\varepsilon_0\omega}\left[ \frac{\sigma_0 \tau_{D0}^{-1}}{\tau_D^{-1}(\omega) - i\omega} + \sigma_{\text{inter}}(\omega) \right]. \quad (6)
$$

### B. Transport properties

Here, we calculate the temperature-dependent lifetimes and mean-free paths of hot carriers accounting for electron-electron and electron-phonon scattering.

For the electron-electron scattering contribution, we calculate the electron-electron scattering rate from the imaginary part of the quasiparticle self-energy within the RPA as [40,41]

$$
(\tau_{\mathbf{k}n}^{e-e})^{-1} = \frac{2}{\hbar} \text{Im} \sum_{\mathbf{k}n}^{e-e}
$$
$$
= \frac{2}{\hbar} \int_{BZ} \frac{d\mathbf{k}'}{(2\pi)^d} \sum_{n'} \sum_{GG'} \tilde{\rho}_{\mathbf{k}n\mathbf{k}'n'}(\mathbf{G}) \tilde{\rho}_{\mathbf{k}n\mathbf{k}'n'}^*(\mathbf{G}')
$$
$$
\times \frac{4\pi e^2}{|\mathbf{k}' - \mathbf{k} + \mathbf{G}|^2} \text{Im}\big[\varepsilon_{\mathbf{GG}'}^{-1}(\mathbf{k}' - \mathbf{k}, \varepsilon_{\mathbf{k}n} - \varepsilon_{\mathbf{k}'n'})\big],
$$
$$
(7)
$$

where $\text{Im} \sum_{\mathbf{k}n}^{e-e}$ is the carrier linewidth due to electron-electron scattering; $\tilde{\rho}_{\mathbf{k}n\mathbf{k}'n'}$ is the density matrix expressed in the plane-wave basis, and $\varepsilon_{\mathbf{GG}'}^{-1}$ is the RPA dielectric matrix for reciprocal lattice vectors $\mathbf{G}$ and $\mathbf{G}'$. According to the Fermi-liquid theory for electrons, the temperature dependence of electron-electron scattering rate is approximated with an analytical correction as [14,42]

$$
(\tau_{\mathbf{k}n}^{e-e})^{-1}(\varepsilon_{\mathbf{k}n}, T_e) \approx \frac{D_e}{\hbar}[(\varepsilon_{\mathbf{k}n} - \varepsilon_F)^2 + (\pi k_B T_e)^2],
$$

where $D_e$ is the constant of proportionality, by fitting Eq. (6) at room temperature $T_0$, and then adds $(D_e/\hbar)(\pi k_B)^2(T_e^2 - T_0^2)$ to Eq. (6) for finite temperature $T_e$.
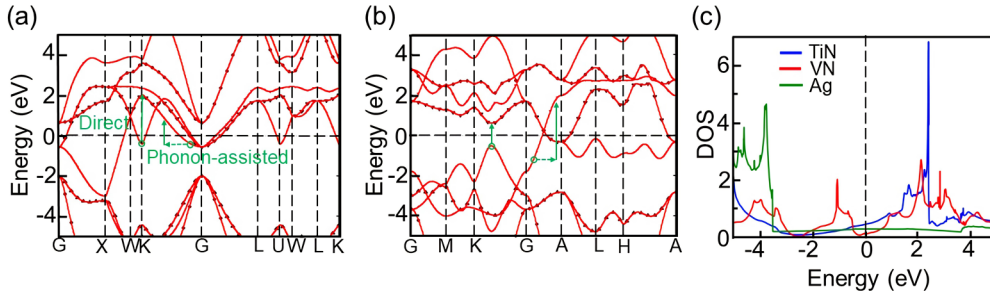


FIG. 2. Band structures of TiN (a) and VN (b). The black scatters represent band structures calculated by the DFT calculation. The red lines are obtained through interpolation of MLWFs. (c) Density of states (DOS) of TiN, VN, and bulk Ag with the unit of states/(eV*volume*atom). The Fermi energies in (a), (b), and (c) are set to 0 eV.
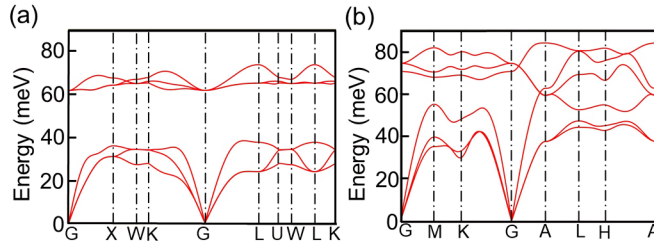
FIG. 3. Phonon spectra of TiN (a) and VN (b).

For the electron-phonon scattering contribution, we calculate the temperature-dependent electron-phonon scattering rate as follow: [43,44]

$$
\left(\tau_{\mathbf{k}n}^{e-ph}\right)^{-1} = \frac{2}{\hbar} \text{Im} \sum_{\mathbf{k}n}^{e-ph}
$$

$$
= \frac{2}{\hbar} \sum_{n'\alpha} \int_{BZ} \frac{\Omega d(\mathbf{k}+\mathbf{q})}{(2\pi)^d} \left| g_{(\mathbf{k}+\mathbf{q})n',\mathbf{k}n}^{\mathbf{q},\alpha} \right|^2
$$

$$
\times \text{Im} \left[ \frac{n_{\mathbf{q},\alpha} + 1 - f_{\mathbf{k}n'}}{\varepsilon_{\mathbf{k}n} - \varepsilon_{(\mathbf{k}+\mathbf{q})n'} - \hbar\omega_{\mathbf{q},\alpha} - i\eta} + \right.
$$

$$
\left. \times \frac{n_{\mathbf{q},\alpha} + f_{\mathbf{k}n'}}{\varepsilon_{\mathbf{k}n} - \varepsilon_{(\mathbf{k}+\mathbf{q})n'} + \hbar\omega_{\mathbf{q},\alpha} - i\eta} \right], \qquad (8)
$$

where $\text{Im} \sum_{\mathbf{k}n}^{e-ph}$ is the carrier linewidth due to electron-phonon scattering; $\eta$ is a small Lorentzian broadening; $n_{\mathbf{q},\alpha}$ is the Bose occupation of phonon state with wave vector $\mathbf{q}$ and polarization index $\alpha$. The temperature dependence of Eq. (7) is embedded in the Fermi occupation of electron state $f_{\mathbf{k}n} = f(\varepsilon_{\mathbf{k}n}, T_e)$ and Bose occupation of phonon state $n_{\mathbf{q}\alpha} = n(\varepsilon_{\mathbf{q}\alpha}, T_e)$. For the integral calculation in Eq. (7), we use $2 \times 10^5$ Monte Carlo sampling points to ensure convergence of the results.

Finally, taking into account the electron-electron and electron-phonon scattering contributions, the carrier lifetime is calculated by $\tau_{\mathbf{k}n} = \frac{\hbar}{2(\text{Im}\sum_{\mathbf{k}n}^{e-e} + \text{Im}\sum_{\mathbf{k}n}^{e-ph})}$, where $\text{Im}\sum_{\mathbf{k}n}^{e-e} + \text{Im}\sum_{\mathbf{k}n}^{e-ph}$ is the total carrier linewidth. Meanwhile, the mean-free path is calculated by $\lambda_{\mathbf{k}n} = v_{\mathbf{k}n} \cdot \tau_{\mathbf{k}n}$, where $\tau_{\mathbf{k}n}$ and $v_{\mathbf{k}n}$ are lifetime and group velocity of hot carriers in the electronic state $\mathbf{k}n$, respectively.

## III. RESULTS AND DISCUSSION

### A. Structure and stability

In this work, we mainly focus on two typical transition metal nitrides, titanium nitride (TiN) and vanadium nitride (VN). As shown in Fig. 1(a), the most stable TiN crystal

is a face-centered cubic structure, and the calculated lattice parameters are $a = b = c = 4.25$ Å. For VN crystal, the mechanically stable structure is the more complex hexagonal phase [Fig. 1(b)] with lattice constants $a = b = 2.74$ Å, and $c = 2.65$ Å, respectively. Figures 2(a) and 2(b) show the band structures of TiN and VN, where the allowed inter- and intraband electronic transitions are marked by green arrows. Meanwhile, Fig. 2(c) shows that TiN has the largest density of electronic states near the Fermi energy, indicating that TiN may sustain plasmon in the visible range, which is particularly desirable for optical devices. In addition, Figs. 3(a) and 3(b) show that the phonon spectra have no imaginary frequencies, indicating the dynamical stabilities of the TiN and VN crystal structures. Physically, electron transitions and electron-phonon interactions exhibit strong temperature dependence. Therefore, this work systematically investigates the surface plasmon and hot carrier properties of TiN and VN at different temperatures.

### B. Plasmonic responses of metallic materials

In general, the plasmonic responses of metallic materials consist mainly of the contributions of Drude resistance, phonon-assisted intraband-, and direct interband electronic transitions. We start with *ab initio* calculations of Drude resistance, which generates thermal effects and competes with intraband electronic transitions at low frequencies. For Drude resistance effects, Table I shows the calculated Fermi velocity, and the ratio $(\sigma_0/\tau_{D0})$ of DC conductivity to the average Drude momentum relaxation time at room temperature, which are closer to the data in Ref. [27]. The results show that the Fermi velocity of VN is lower than that of TiN, and both are lower than that of Ag (about $1.4 \times 10^6$ ms$^{-1}$). Combined with the lowest density of states of VN near Fermi energy shown in Fig. 2(c), we can infer that the carrier lifetime in VN is longer than that of Ag due to the smaller electron-phonon scattering effect. In addition, from the real part of complex conductivity Re$\sigma(\omega)$ in Eq. (1), the larger value of the ratio $(\sigma_0/\tau_{D0})$ indicates that the Drude resistance effect contributes more to the surface plasmon decay at low frequencies. Table I shows that the ratio $(\sigma_0/\tau_{D0})$ in TiN and VN is almost independent of temperature.

According to Eqs. (3) and (4), we then calculate the momentum relaxation times of phonon-assisted intraband electronic transitions and the imaginary part of the dielectric function due to direct interband electronic transitions, which are two important components of the plasmonic response of metallic materials. Specifically, the momentum relaxation time directly determines the intraband loss due to the phonon-assisted electronic transitions. As shown in Fig. 4, similar to

TABLE I. Comparison of calculated parameter values with those in reference.

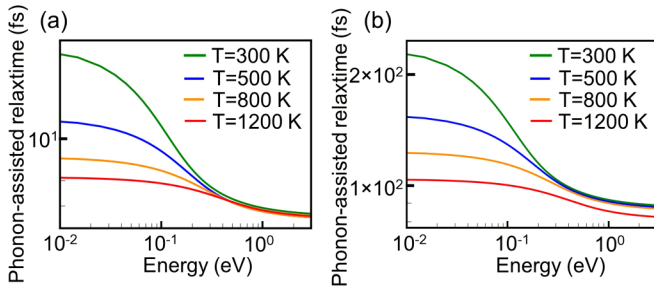| | TiN (300 K) | | VN (300 K) | |
|---|---|---|---|---|
| | Ref. [27] | Calculated | Ref. [27] | Calculated |
| Fermi velocity ($10^6$ ms$^{-1}$) | 0.72 | 0.72 | 0.28 | 0.28 |
| $\sigma_0/\tau_{D0}$ [1/(nΩ m fs)] | 0.001 | 0.004 | $5.29 \times 10^{-5}$ | $1.43 \times 10^{-5}$ |

FIG. 4. Momentum relaxation times of phonon-assisted intraband electronic transitions, as a function of photon energy, in TiN (a) and VN (b) at 300, 500, 800, and 1200 K.



FIG. 6. Real part of the optical conductivity $\mathrm{Re}\sigma(\omega)$ as a function of photon energy in TiN (a) and VN (b) at 300, 500, 800, and 1200 K.

the graphene [33], the momentum relaxation time in TiN (VN) drops dramatically at frequencies above 0.06 (0.08) eV, due to strong scattering with optical phonons with a maximum energy $\sim 0.074$ (0.085) eV shown in Fig. 3. Meanwhile, the momentum relaxation times of VN are one order of magnitude higher than that of TiN, indicating the lower intraband loss of VN at low energies. Notably, the temperature dependence of the momentum relaxation times is concentrated within about 1 eV. With an increase in temperature, the momentum relaxation times at low energies decrease significantly. As shown in Fig. 5, the imaginary part of the dielectric function directly quantifies the surface plasmon decay due to interband electronic transitions with energies above the optical gap in TiN and VN. Observably, the temperature has a weak effect on the imaginary part of dielectric functions of TiN and VN at energies below about 1 eV. Consequently, the main temperature effect on the dielectric response of TiN and VN exhibits a significant intraband and interband response at low energies. In addition, in Fig. 6 we plot the frequency-dependent conductivity at four temperatures. It is shown that temperature mainly affects conductivity at low frequencies. It is noteworthy that TiN still has excellent conductivity at higher temperatures, which is very close to that of Ag ($6.25 \times 10^5 \ \Omega^{-1} \, \mathrm{cm}^{-1}$) at room temperature. Based on electromagnetic theory, the corresponding temperature-dependent dielectric function $\varepsilon(\omega)$ is obtained from Eq. (5), followed by further discussion of the direct optical absorption and surface plasmon properties of TiN and VN at different temperatures.

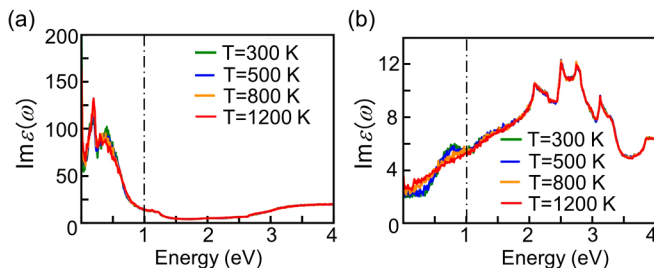We calculate the optical absorption coefficient from single-particle electronic excitations, including the three physical processes discussed above, which is expressed as [45]

$$\alpha(\omega) = \sqrt{2}\frac{\omega}{c}\left[\sqrt{\varepsilon_1^2(\omega) + \varepsilon_2^2(\omega)} - \varepsilon_1(\omega)\right]^{1/2} \qquad (9)$$

where $\varepsilon_1(\omega)$ and $\varepsilon_2(\omega)$ are the real and imaginary parts of the dielectric function $\varepsilon(\omega)$, respectively. The calculated dielectric functions of TiN and VN shown in Fig. 7 are consistent with the results at room temperature in Ref. [26], indicating the reliability of our theoretical calculations. Figure 7(c) shows that TiN maintains efficient optical absorption at different temperatures, even higher than Ag [46], which is beneficial for high-temperature applications. In contrast, the optical absorption coefficients of VN shown in Fig. 7(d) exhibit temperature sensitivity at low energies, as indicated by the blue circle, where the optical absorption coefficients increase with increasing temperature.



FIG. 7. The real and imaginary part of the complex dielectric functions, as a function of photon energy, in TiN (a) and VN (b) at room temperature (300 K), which include the contributions of Drude resistance, direct interband-, and phonon-assisted intraband electronic transitions. The single-particle optical absorption coefficients $\alpha(\omega)$, as a function of photon energy, in TiN (c) and VN (d) at 300, 500, 800, and 1200 K, where the enlarged result shows the energy range marked by the blue circle.



FIG. 5. Imaginary part of the dielectric function $\mathrm{Im}\varepsilon(\omega)$ due to direct interband electronic transitions, as a function of photon energy, in TiN (a) and VN (b) at 300, 500, 800, and 1200 K.
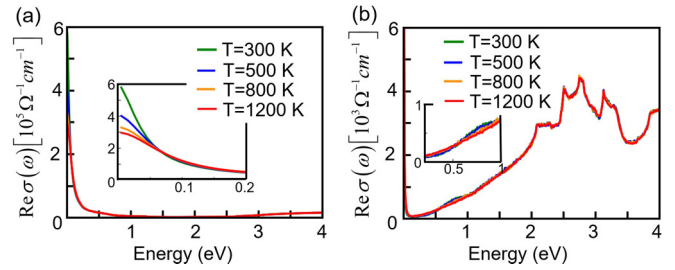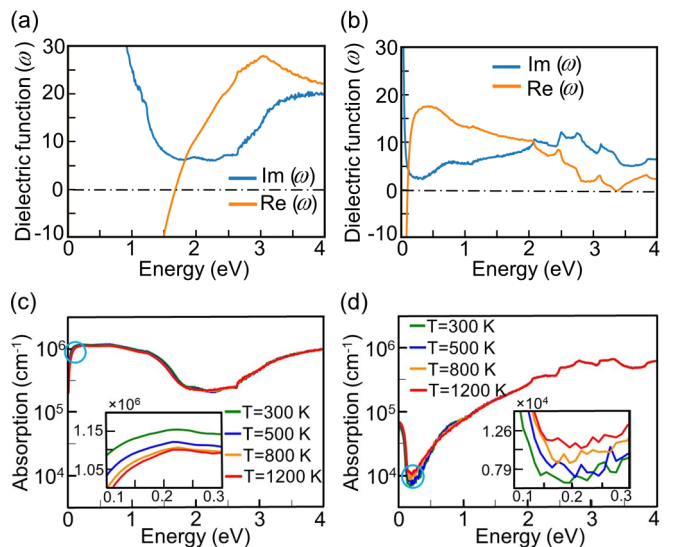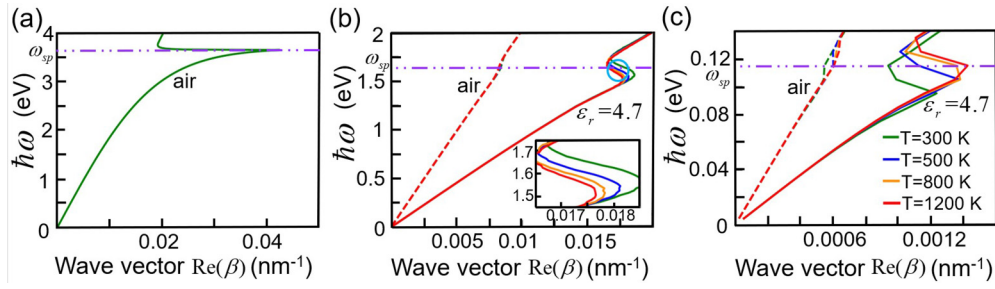
FIG. 8. (a) Plasmon dispersion of bulk Ag at the temperature of 300 K. (b) and (c) show the plasmon dispersion in air environment ($\varepsilon_r = 1$) and AlN dielectrics ($\varepsilon_r = 4.7$) of TiN and VN, respectively, at 300, 500, 800, and 1200 K. The dashed and solid lines in (b) and (c) indicate air environment ($\varepsilon_r = 1$) and AlN dielectrics ($\varepsilon_r = 4.7$), respectively. The energy in (a), (b), and (c) indicates the plasmonic response frequency. The purple line indicates the value of surface plasmon frequency $\omega_{sp}$ at the Ag/TiN/VN–air interface. The enlarged result in (b) shows the energy range marked by the blue circle.

Furthermore, according to Ref. [41], the total plasmon decay rate $\Gamma$ can be determined as

$$\Gamma = \frac{\omega}{2L(\omega)|\gamma(z<0)|}\lambda^* \mathrm{Im}\varepsilon(\omega)\lambda. \quad (10)$$

Here, $\mathrm{Im}\varepsilon(\omega)$ is the imaginary part of the calculated dielectric function obtained from Eq. (5); $L(\omega)$ is the quantization length for the plasmon determined by normalizing the energy density of the mode; $|\gamma(z<0)|$ is the inverse decay length of the plasmon into the metal, and $\lambda$ is the polarization vector.

### C. Surface plasmon properties

In this section, we analyze the surface plasmon properties at the TiN/VN–dielectric interface. The surface plasmon excitation at the semi-infinite interface corresponds to the poles of the Fresnel reflection coefficient $r_{TM}$ [47]:

$$r_{TM} = \frac{\varepsilon(\omega)k_{\perp}^+ - \varepsilon_r k_{\perp}^-}{\varepsilon(\omega)k_{\perp}^+ + \varepsilon_r k_{\perp}^-}, \quad (11)$$

where $\varepsilon(\omega)$ is the dielectric functions of TiN and VN; the dielectric constant $\varepsilon_r$ defines the adjacent dielectric environment; $k_{\perp}^{\pm}$ is the propagation constants of the reflected incident light. Thus, the plasmon dispersion (frequency $\omega$ versus wave vector $\beta$) is calculated as [7,48]

$$\beta = k_0 \sqrt{\frac{\varepsilon_r \varepsilon(\omega)}{\varepsilon_r + \varepsilon(\omega)}}, \quad (12)$$

where $k_0 \equiv \frac{\omega}{c}$ is the free-space wave vector and $c$ is the speed of light in a vacuum. In the long-wavelength limit, the electric polarization will completely shield the external electric field, which means that the dielectric function $\varepsilon(\omega)$ becomes much larger than the dielectric constant $\varepsilon_r$, that is, $\varepsilon(\omega) \gg \varepsilon_r$. Therefore, the plasmon dispersion of Surface Plasmon Polariton (SPP) at the interface between the two half spaces is close to $k_0$ at the light line [49].

Figure 8 shows the plasmon dispersion [frequency $\omega$ versus wave vector $\mathrm{Re}(\beta)$] of TiN and VN. As a comparison, bulk Ag [Fig. 8(a)] in the air ($\varepsilon_r = 1$) exhibits a wide energy window of about 3.6 eV at 300 K and has a wave vector of the bound SPP close to about 0.04 nm$^{-1}$. Theoretically, the energy window range of negative $\mathrm{Re}\varepsilon(\omega)$ in the dielectric function shown in Fig. 7 is related to the surface plasmon response

range. The wide range of negative $\mathrm{Re}\varepsilon(\omega)$ and the corresponding low $\mathrm{Im}\varepsilon(\omega)$ in metallic material indicate excellent plasmonic behavior over a broad surface plasmon frequency range. Therefore, as shown in Figs. 8(b) and 8(c), the surface plasmon frequency of TiN is about 1.61 eV, indicating that the plasmonic behavior of TiN extends to the visible region. In contrast, VN exhibits a much narrower plasmonic window, less than 0.12 eV. In particular, as the temperature increases, the surface plasmon frequency is redshifted for TiN and blueshifted for VN, accompanied by a decrease in the SPP wave vector in TiN and an increase in VN. In addition, our results indicate that the air environment is difficult to maintain stable and sharp SPP performances. Therefore, strong SPP in SPP-based devices requires a dielectric material with increased dielectric constant, such as AlN ($\varepsilon_r = 4.7$) [50,51].

To evaluate the application potential of the SPP at the TiN/VN–dielectric interface, we calculate two distinct figures of merit [52]: one is effective propagation length with the ratio $\frac{\mathrm{Re}(\beta)}{\mathrm{Im}(\beta)}$, which measures the SPP propagation length before an SPP loss of most of its energy. The other is confinement ratio $\frac{\lambda_{\mathrm{air}}}{\lambda_{sp}}$ ($\lambda_{\mathrm{air}} = \frac{2\pi c}{\omega}$, $\lambda_{sp} = \frac{2\pi}{\mathrm{Re}(\beta)}$), which reflects the degree of localization. As shown in Figs. 9(a), 9(b), and 9(c), in the entire surface plasmonic response range, the effective propagation lengths of TiN and VN are larger than that of bulk Ag, indicating a low SPP loss of TiN and VN. With the increase of temperature, the SPP loss increases slightly for TiN and decreases significantly for VN. Meanwhile, Figs. 9(d), 9(e), and 9(f) show that TiN and VN exhibit confinement ratios close to 1 at different temperatures, which is comparable to that of bulk Ag. Therefore, TiN is an excellent alternative to noble metals for low-loss and broadband plasmonic applications at different temperatures. Meanwhile, VN with a low SPP loss is mainly suitable for photoelectric conversion in the infrared range at different temperatures. In addition, the results show that increasing the dielectric constant of the dielectric significantly reduces the effective propagation length and increases the confinement of the SPP at the TiN/VN–dielectric interface.

### D. Hot carrier properties

Due to the excellent optical absorption and surface plasmon properties of TiN and VN discussed in the previous
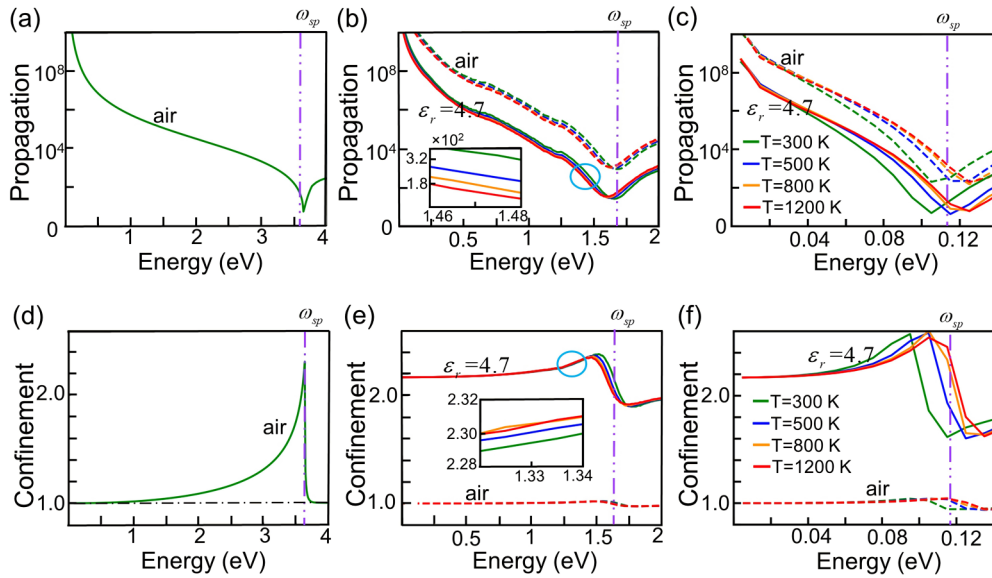
FIG. 9. Effective propagation length ($\frac{\text{Re}(\beta)}{\text{Im}(\beta)}$) for bulk Ag (a), TiN (b), and VN (c). Confinement ratio ($\frac{\lambda_{\text{air}}}{\lambda_{sp}}$) for bulk Ag (d), TiN (e), and VN (f). The dashed and solid lines in (b), (c), (e), and (f) indicate air environment ($\varepsilon_r = 1$) and AlN dielectrics ($\varepsilon_r = 4.7$), respectively. The enlarged result shows the energy range marked by the blue circle. The horizontal axis indicates the plasmonic response frequency. The purple line indicates the value of surface plasmon frequency $\omega_{sp}$ at the Ag/TiN/VN–air interface.

section, their inevitable losses also provide unique opportunities for applications. Especially, the nonradiative plasmon decay generates hot carriers, which offers tremendous opportunities for combining efficient light capture with energy conversion and catalysis at the nanoscale. Therefore, in this section, we comprehensively discuss the properties of photon/plasmon-driven hot carriers of TiN and VN at different temperatures, including their energy distribution and transport ability.

### *Carrier energy dispersions*

In general, there are mainly two microscopic mechanisms for generating hot carriers: direct interband and phonon-assisted intraband electronic transitions. Using the same calculation methods as our previous work [37], we discuss the energy dispersion of hot carriers generated by direct interband and phonon-assisted intraband electronic transitions, respectively.

For hot carriers generated by direct interband electronic transitions, Figs. 10 and 11 show that the carrier energy distributions of TiN and VN are more complex than those of noble metals with uniform carrier energy distributions [41]. The reason is that the energy distribution of hot carriers generated by direct interband electronic transitions is closely related to the electronic structure. Specifically, the carrier energy distribution of TiN with "spiky" distribution probability is asymmetrical, exhibiting high-energy hot holes with photon/plasmon energies above 2.5 eV and high-energy hot electrons with photon/plasmon energies less than 2.5 eV. Meanwhile, as marked by the red rectangle, the temperature affects the carrier energy distribution when the photon/plasmon energy is below 2.5 eV. With the increase in temperature, the distribution probability of hot electrons and hot holes gradually decreases, but their energy distribution is

almost unaffected. In addition, as marked by the red circle, the carrier energy distribution of VN exhibits the symmetric bimodal feature in a very narrow energy range. Meanwhile, the temperature has almost no effect on the energy and probability distribution of hot electrons and hot holes in VN. Significantly, we find that when the photon/plasmon energy is higher than about 2.5 eV, the energy and probability distribution of energetic holes in TiN and energetic electrons in VN exhibit robustness to temperature.

For hot carriers generated by phonon-assisted intraband electronic transitions, Figs. 12 and 13 show that the carrier energy distributions of TiN and VN are relatively flat compared to that from interband electronic transitions. Also, the hot
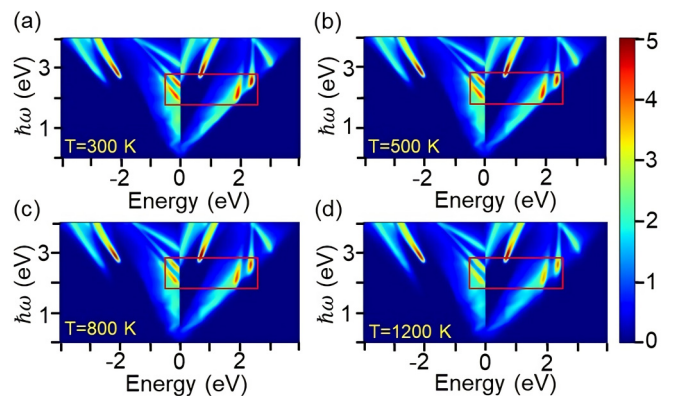


FIG. 10. Energy distribution of hot carriers generated by direct interband electronic transitions, as a function of photon/plasmon energies ($\hbar\omega$), in TiN at 300 (a), 500 (b), 800 (d), and 1200 K (d). The horizontal axis indicates the energy of photon/plasmon-generated carriers, where negative values indicate hot holes and positive values indicate hot electrons. The color bar indicates the distribution probabilities of carriers. The Fermi energy is set to 0 eV.
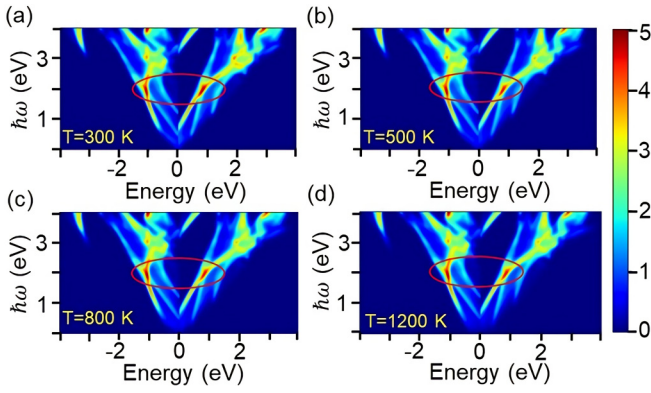
FIG. 11. Energy distribution of hot carriers generated by direct interband electronic transitions, as a function of photon/plasmon energies ($\hbar\omega$), in VN at 300 (a), 500 (b), 800 (c), and 1200 K (d). The horizontal axis indicates the energy of photon/plasmon-generated carriers, where negative values indicate hot holes and positive values indicate hot electrons. The color bar indicates the distribution probabilities of carriers. The Fermi energy is set to 0 eV.

carriers generated by phonon-assisted electronic transitions in TiN and VN are dominated by high-energy hot electrons. In addition, as marked by the red circle, the temperature affects the distribution probability of the hot carriers in VN, where the distribution probability decreases with increasing temperature. Considering the plasmonic frequency range, the energy of the plasmon-driven hot carriers will be smaller than the maxima of allowed surface plasmon excitation energies, which are 1.6 eV for TiN and 0.12 eV VN, respectively. In this energy region, TiN exhibits temperature-sensitive energetic electrons, while VN is temperature-sensitive energetic holes excited by phonon-assisted electronic transitions.

For the single-particle (particle-hole mode) region, from Figs. 10 and 11, the incident energy onset of single particles generated by interband electronic transitions in TiN and VN
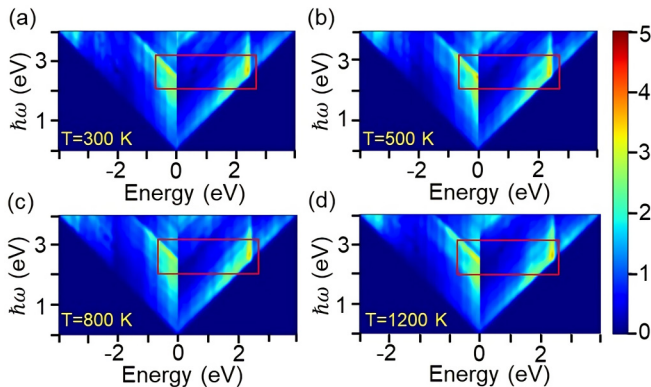


FIG. 12. Energy distribution of hot carriers generated by phonon-assisted intraband electronic transitions, as a function of photon/plasmon energies ($\hbar\omega$), in TiN at 300 (a), 500 (b), 800 (c), and 1200 K (d). The horizontal axis indicates the energy of photon/plasmon-generated carriers, where negative values indicate hot holes and positive values indicate hot electrons. The color bar indicates the distribution probabilities of carriers. The Fermi energy is set to 0 eV.
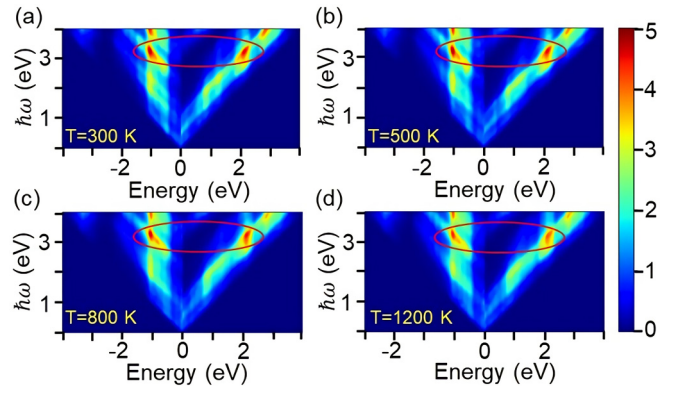


FIG. 13. Energy distribution of hot carriers generated by phonon-assisted intraband electronic transitions, as a function of photon/plasmon energies ($\hbar\omega$), in VN at 300 (a), 500 (b), 800 (c), and 1200 K (d). The horizontal axis indicates the energy of photon/plasmon-generated carriers, where negative values indicate hot holes and positive values indicate hot electrons. The color bar indicates the distribution probabilities of carriers. The Fermi energy is set to 0 eV.

is about 0.2 and 0.7 eV, respectively. From Figs. 12 and 13, the energy onset of single particles generated by intraband electronic transitions in both TiN and VN starts almost from 0 eV. Therefore, the single-particle (particle-hole mode) energy region overlaps the surface plasmon region, indicating that the surface plasmon decay can occur by Landau damping.

### E. Transport properties

Considering the electron-electron and electron-phonon scattering processes, we calculate the lifetimes and mean-free paths of hot carriers to quantitatively analyze the temperature effect on the transport properties of hot carriers.

Figure 14 shows the carrier linewidths caused by electron-electron scattering and electron-phonon scattering, respectively, at different temperatures. As expected for a normal metal conforming to Fermi-liquid theory, electron-electron scattering dominates far away from the Fermi energy. Meanwhile, the large value of carrier linewidths is confirmed to be from interband impact ionization and Auger recombination processes. In addition, electron-phonon scattering dominates near the Fermi energy, where the linewidth value of electron-electron scattering reaches the minimum at the Fermi energy. Note that the carrier linewidth of electron-phonon scattering is comparable to that of electron-electron scattering. This indicates that electron-phonon scattering is also important enough to not neglect its role in hot carrier transport, which is different from the assumption that electron-phonon scattering occurs on a very slow timescale [53]. More importantly, our results show that the temperature has a greater effect on electron-phonon scattering than on electron-electron scattering. This is because as the temperature increases, the collision between free electrons and the crystal lattice becomes stronger. In addition, the temperature has a significant effect on the carrier linewidth of VN compared to TiN. For example, the carrier linewidth in VN near the Fermi energy increases from 4 meV
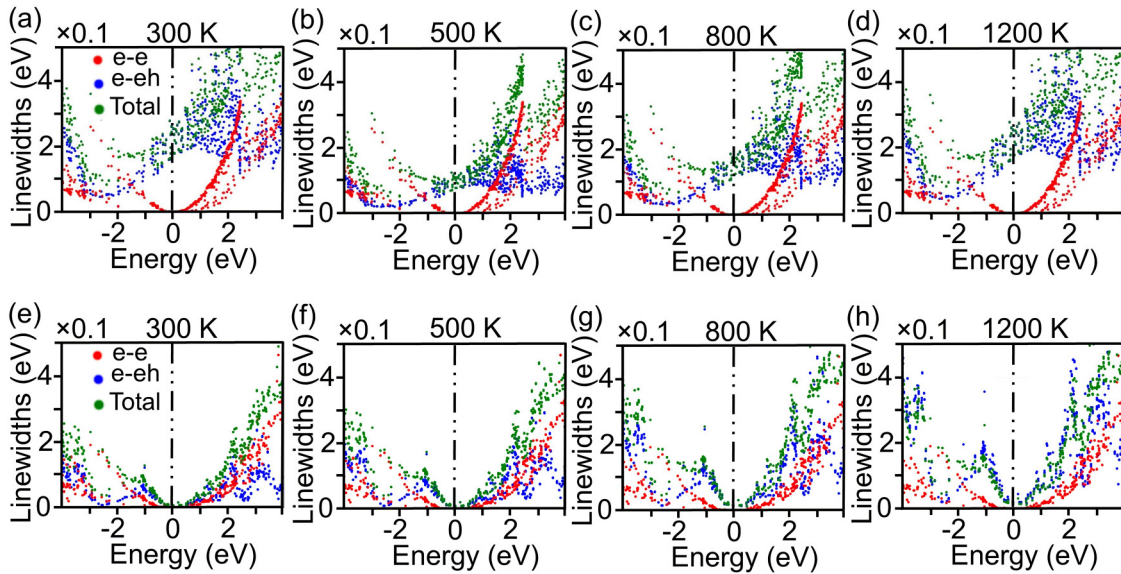
FIG. 14. Carrier linewidths in TiN at 300 (a), 500 (b), 800 (c), and 1200 K (d). Carrier linewidths in VN at 300 (e), 500 (f), 800 (g), and 1200 K (h). The red, blue, and green scattering points represent the carrier linewidths with electron-electron scattering, electron-phonon scattering, and total scattering effects, respectively. The horizontal axis indicates the energy of photon/plasmon-generated hot carriers, where negative values indicate hot holes and positive values indicate hot electrons. The Fermi energy is set to 0 eV, which is marked by the black dotted-dashed line.

at 300 K to 15 meV at 1200 K, which is almost four times higher than that at room temperature. However, as the temperature increases from 300 to 1200 K, the carrier linewidth in TiN increases only from 78 to 200 meV.

Excellent plasmonic materials require high-energy hot carriers with long lifetimes and transport distances, which are being actively explored for high-temperature hot carrier devices. Here, our results show that VN has a maximum lifetime of 53 fs at 300 K, which is much longer than that of conventional plasmonic materials (Au, Ag) [41]. It is worth noting that the maximum carrier lifetime in VN at 1200 K is still comparable to that in noble metals at room temperature, and even higher than that in Al [41]. In particular, the results show that the lifetimes of high-energy hot holes in TiN and VN are longer than those of high-energy hot electrons. For example, as shown in Figs. 15(a) and 15(e), the lifetime of high-energy hot holes in TiN (VN) reaches 3.2(2.0) fs at energies between −4 and −3 eV, but that of high-energy hot electrons is 1.1(1.1)
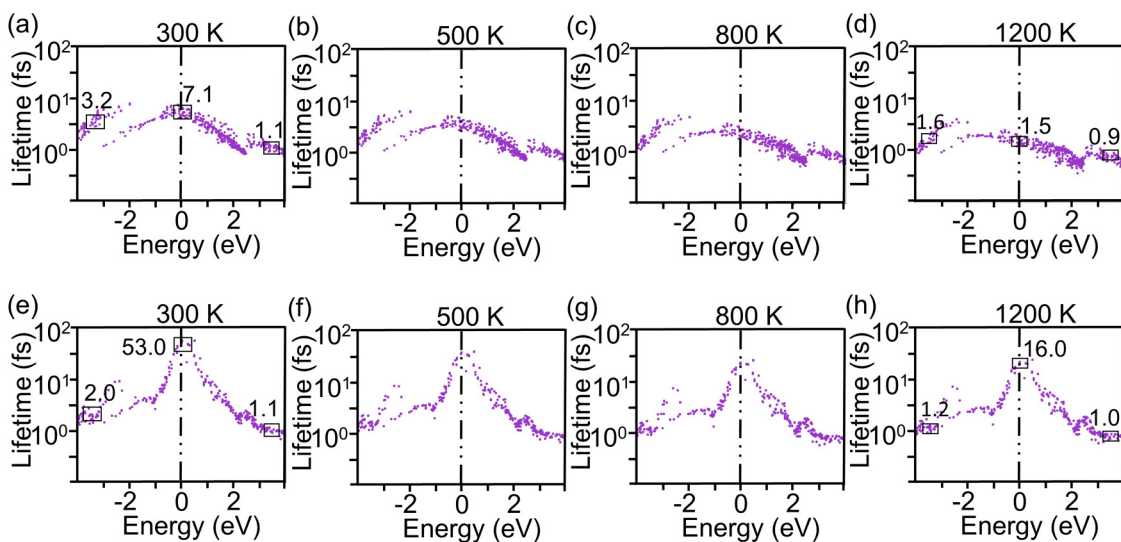


FIG. 15. Carrier lifetimes, accounting for electron-electron and electron-phonon scattering contributions in TiN at 300 (a), 500 (b), 800 (c), and 1200 K (d). Carrier lifetimes, accounting for electron-electron and electron-phonon scattering contributions in VN at 300 (e), 500 (f), 800 (g), and 1200 K (h). The horizontal axis indicates the energy of photon/plasmon-generated hot carriers, where negative values indicate hot holes and positive values indicate hot electrons. The Fermi energy is set to 0 eV, which is marked by the black dotted dashed line.
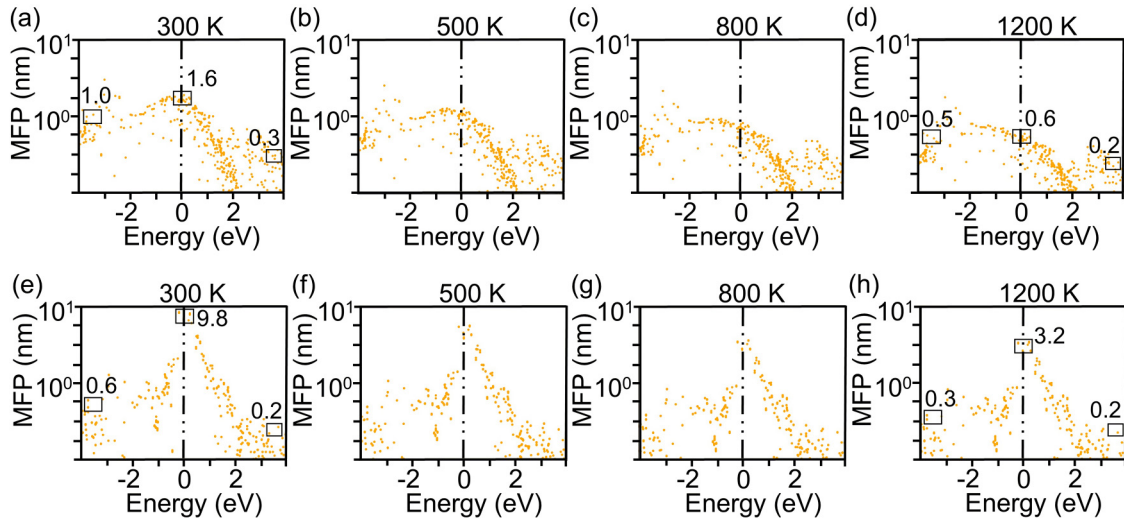
FIG. 16. Mean-free paths (MFP) of hot carriers, accounting for electron-electron and electron-phonon scattering contributions in TiN at 300 (a), 500 (b), 800 (c), and 1200 K (d). MFP of hot carriers, accounting for electron-electron and electron-phonon scattering contributions in VN at 300 (e), 500 (f), 800 (g), and 1200 K (h). The horizontal axis indicates the energy of photon/plasmon-generated hot carriers, where negative values indicate hot holes and positive values indicate hot electrons. The Fermi energy is set to 0 eV, which is marked by the black dotted-dashed line.

fs at energies between 3 and 4 eV. Meanwhile, the high temperature has a greater effect on high-energy hot holes than on high-energy hot electrons. For example, the lifetime of high-energy hot holes in TiN (VN) decreases from 3.2(2.0) fs at 300 K to 1.6(1.2) at 1200 K fs, but that of high-energy hot electrons is almost constant. Meanwhile, as shown in Fig. 16, the mean-free path of high-energy hot holes in TiN (VN) decreases from 1.0(0.6) nm at 300 K to 0.5(0.3) nm at 1200 K, but that of high-energy hot electrons is always about 0.2 nm. Therefore, the energetic holes of TiN with long lifetimes and transport distances exhibit strong temperature sensitivity, making it an excellent plasmonic material for carrier-based temperature-sensing devices. Meanwhile, the energy dispersion and transport properties of energetic electrons of VN are almost temperature independent, which is of great significance for carrier-based applications.

## IV. CONCLUSIONS

In summary, based on the first-principles calculations, we systematically investigate the surface plasmon and hot carrier properties of TiN and VN at different temperatures. By quantifying the three main microscopic processes of dielectric response in TiN and VN, we find that the temperature mainly affects the intraband response at low energies, and hardly affects the interband electronic transition process at high energies. The optical absorption coefficients of TiN and VN remain up to $10^6$ $cm^{-1}$ at different temperatures, even higher than Ag. Meanwhile, TiN and VN exhibit low surface plasmon loss comparable to that of Ag at different

temperatures. Particularly, the low-loss TiN has a broad surface plasmon response that extends to visible light, and the low-loss VN exhibits a much narrower plasmonic window, less than 0.12 eV. With the increase of temperature, the surface plasmon frequency is redshifted for TiN and blueshifted for VN, accompanied by a decrease in the SPP wave vector in TiN and an increase in VN. In terms of hot carriers, the energy and probability distributions of high-energy hot holes in TiN and high-energy hot electrons in VN exhibit thermal stability under high-energy incident light. Meanwhile, the results show that high temperatures significantly decrease the carrier lifetimes and mean-free paths of TiN and VN. However, VN still has a maximum lifetime of 16 fs at high temperatures, which is comparable to that of Al at room temperature, indicating the promise of efficient carrier extraction at high temperatures. In addition, the temperature effect on high-energy hot holes is significantly higher than that on high-energy hot electrons. We expect that the reported results will provide theoretical guidance for the design of the next high-temperature plasmonic devices. Furthermore, the theoretical method introduced here is general, and will facilitate the exploration of the temperature-dependent plasmonic response and carrier properties of discovered materials.

[1] H. Su, S. Wu, Y. Yang, Q. Leng, L. Huang, J. Fu, Q. Wang, H. Liu, and L. Zhou, Surface plasmon polariton-enhanced photoluminescence of monolayer MoS$_2$ on suspended periodic metallic structures, Nanophotonics **10**, 975 (2020).

[2] G. Tagliabue, A. S. Jermyn, R. Sundararaman, A. J. Welch, J. S. DuChene, R. Pala, A. R. Davoyan, P. Narang, and H. A. Atwater, Quantifying the role of surface plasmon excitation and hot carrier transport in plasmonic devices, Nat. Commun. **9**, 3394 (2018).

[3] S. Li, P. Miao, Y. Zhang, J. Wu, B. Zhang, Y. Du, X. Han, J. Sun, and P. Xu, Recent advances in plasmonic nanostructures for enhanced photocatalysis and electrocatalysis, Adv. Mater. **33**, 2000086 (2021).

[4] M. Sakamoto, T. Kawawaki, M. Kimura, T. Yoshinaga, J. J. M. Vequizo, H. Matsunaga, C. S. K. Ranasinghe, A. Yamakata, H. Matsuzaki, A. Furube, and T. Teranishi, Clear and transparent nanocrystals for infrared-responsive carrier transfer, Nat. Commun. **10**, 406 (2019).

[5] R. A. Maniyara, D. Rodrigo, R. Yu, J. Canet-Ferrer, D. S. Ghosh, R. Yongsunthon, D. E. Baker, A. Rezikyan, F. J. García de Abajo, and V. Pruneri, Tunable plasmons in ultrathin metal films, Nat. Photonics **13**, 328 (2019).

[6] A. Boltasseva and H. A. Atwater, Low-loss plasmonic metamaterials, Science **331**, 290 (2011).

[7] W. P. Guo, R. Mishra, C. W. Cheng, B. H. Wu, L. J. Chen, M. T. Lin, and S. Gwo, Titanium nitride epitaxial films as a plasmonic material platform: Alternative to gold, ACS Photonics **6**, 1848 (2019).

[8] H. Reddy, U. Guler, Z. Kudyshev, A. V. Kildishev, V. M. Shalaev, and A. Boltasseva, Temperature-dependent optical properties of plasmonic titanium nitride thin films, ACS Photonics **4**, 1413 (2017).

[9] W. Wang, H. Wang, P. Yu, K. Sun, X. Tong, F. Lin, C. Wu, Y. You, W. Xie, Y. Li, C. Yuan, A. O. Govorov, O. L. Muskens, H. Xu, S. Sun, and Z. Wang, Broadband thin-film and metamaterial absorbers using refractory vanadium nitride and their thermal stability, Opt. Express **29**, 33456 (2021).

[10] X. Wang, J. Jian, S. Diaz-Amaya, C. E. Kumah, P. Lu, J. Huang, D. G. Lim, V. G. Pol, J. P. Youngblood, A. Boltasseva, L. A. Stanciu, D. M. O'Carroll, X. Zhang, and H. Wang, Hybrid plasmonic Au-TiN vertically aligned nanocomposites: A nanoscale platform towards tunable optical sensing, Nanoscale Adv. **1**, 1045 (2019).

[11] H. Hu, F. Zhai, D. Hu, Z. Li, B. Bai, X. Yang, and Q. Dai, Broadly tunable graphene plasmons using an ion-gel top gate with low control voltage, Nanoscale **7**, 19493 (2015).

[12] S. N. Shirodkar, M. Mattheakis, P. Cazeaux, P. Narang, M. Soljačić, and E. Kaxiras, Quantum plasmons with optical-range frequencies in doped few-layer graphene, Phys. Rev. B **97**, 195435 (2018).

[13] J. Kim, G. Lee, S. G. Menabde, Y. J. Cho, C. Rockstuhl, and M. S. Jang, Temperature-dependent plasmonic response of graphene nanoresonators, ACS Photonics **9**, 2256 (2022).

[14] C. A. C. Garcia, J. Coulter, and P. Narang, Optoelectronic response of the type-I weyl semimetals TaAs and NbAs from first principles, Phys. Rev. Res. **2**, 013073 (2020).

[15] G. Gumbs, A. Iurov, J. Y. Wu, M. F. Lin, and P. Fekete, Plasmon excitations of multi-layer graphene on a conducting substrate, Sci. Rep. **6**, 21063 (2016).

[16] G. Gumbs, N. J. M. Horing, A. Iurov, and D. Dahal, Plasmon excitations for encapsulated graphene, J. Phys. D: Appl. Phys. **49**, 225101 (2016).

[17] A. Iurov, L. Zhemchuzhna, G. Gumbs, D. Huang, D. Dahal, and Y. Abranyos, Finite-temperature plasmons, damping, and

[18] collective behavior in the model, Phys. Rev. B **105**, 245414 (2022).

[18] A. Iurov, G. Gumbs, D. Huang, and G. Balakrishnan, Thermal plasmons controlled by different thermal-convolution paths in tunable extrinsic dirac structures, Phys. Rev. B **96**, 245403 (2017).

[19] A. Iurov, L. Zhemchuzhna, G. Gumbs, D. Huang, P. Fekete, F. Anwar, D. Dahal, and N. Weekes, Tailoring plasmon excitations in armchair nanoribbons, Sci. Rep. **11**, 20577 (2021).

[20] A. Iurov, D. Huang, G. Gumbs, W. Pan, and A. A. Maradudin, Effects of optical polarization on hybridization of radiative and evanescent field modes, Phys. Rev. B **96**, 081408(R) (2017).

[21] E. Cortes, W. Xie, J. Cambiasso, A. S. Jermyn, R. Sundararaman, P. Narang, S. Schlucker, and S. A. Maier, Plasmonic hot electron transport drives nano-localized chemistry, Nat. Commun. **8**, 14880 (2017).

[22] Y. J. Jang, K. Chung, J. S. Lee, C. H. Choi, J. W. Lim, and D. H. Kim, Plasmonic hot carriers imaging: Promise and outlook, ACS Photonics **5**, 4711 (2018).

[23] R. Kamarudheen, G. W. Castellanos, L. P. J. Kamp, H. J. H. Clercx, and A. Baldi, Quantifying photothermal and hot charge carrier effects in plasmon-driven nanoparticle syntheses, ACS Nano **12**, 8447 (2018).

[24] D. K. Patel and K. N Vyas, Temperature dependence electron-impurity scattering rate in doped bilayer graphene, Adv. Mater. Res. **665**, 154 (2013).

[25] D. K. Efetov and P. Kim, Controlling Electron-phonon Interactions in Graphene at Ultrahigh Carrier Densities, Phys. Rev. Lett. **105**, 256805 (2010).

[26] K. Setoura and S. Ito, Quantifying the durability of transition metal nitrides in thermoplasmonics at the single-nanoparticle level, AIP Adv. **11**, 115027 (2021).

[27] A. Habib, F. Florio, and R. Sundararaman, Hot carrier dynamics in plasmonic transition metal nitrides, J. Opt. **20**, 064001 (2018).

[28] R. Sundararaman, K. Letchworth-Weaver, K. A. Schwarz, D. Gunceler, Y. Ozhabes, and T. A. Arias, JDFTx: Software for joint density-functional theory, SoftwareX **6**, 278 (2017).

[29] E. Kioupakis, P. Rinke, A. Schleife, F. Bechstedt, and C. G. Van de Walle, Free-carrier absorption in nitrides from first principles, Phys. Rev. B **81**, 241201 (2010).

[30] M. Schlipf and F. Gygi, Optimization algorithm for the generation of ONCV pseudopotentials, Comput. Phys. Commun. **196**, 36 (2015).

[31] I. Souza, N. Marzari, and D. Vanderbilt, Maximally localized Wannier functions for entangled energy bands, Phys. Rev. B **65**, 035109 (2001).

[32] F. Giustino, M. L. Cohen, and S. G. Louie, Electron-phonon interaction using Wannier functions, Phys. Rev. B **76**, 165108 (2007).

[33] R. Sundararaman, T. Christensen, Y. Ping, N. Rivera, J. D. Joannopoulos, M. Soljačić, and P. Narang, Plasmonics in argentene, Phys. Rev. Mater. **4**, 074011 (2020).

[34] A. Vakil and N. Engheta, Transformation optics using graphene, Science **332**, 1291 (2011).

[35] D. Haberer, L. Petaccia, A. V. Fedorov, C. S. Praveen, S. Fabris, S. Piccinin, O. Vilkov, D. V. Vyalikh, A. Preobrajenski, N. I. Verbitskiy, H. Shiozawa, J. Fink, M. Knupfer, B. Büchner, and A. Grüneis, Anisotropic Eliashberg function and

electron-phonon coupling in doped graphene, Phys. Rev. B **88**, 081401 (2013).

[36] P. B. Allen, Electron-phonon effects in the infrared properties of metals, Phys. Rev. B **3**, 305 (1971).

[37] C. Jian, J. Zhang, W. He, and X. Ma, Au-Al intermetallic compounds: A series of more efficient LSPR materials for hot carriers-based applications than noble metal Au, Nano Energy **82**, 105763 (2021).

[38] R. Sundararaman, P. Narang, A. S. Jermyn, W. A. Goddard, 3rd, and H. A. Atwater, Theoretical predictions for hot-carrier generation from surface plasmon decay, Nat. Commun. **5**, 5788 (2014).

[39] K. S. B. De Silva, A. Gentle, M. Arnold, V. J. Keast, and M. B. Cortie, Dielectric function and its predicted effect on localized plasmon resonances of equiatomic Au-Cu, J. Phys. D: Appl. Phys. **48**, 215304 (2015).

[40] F. Ladstädter, U. Hohenester, P. Puschnig, and C. Ambrosch-Draxl, First-principles calculation of hot-electron scattering in metals, Phys. Rev. B **70**, 235125 (2004).

[41] A. M. Brown, R. Sundararaman, P. Narang, W. A. Goddard, 3rd, and H. A. Atwater, Nonradiative plasmon decay and hot carrier dynamics: Effects of phonons, surfaces, and geometry, ACS Nano **10**, 957 (2016).

[42] A. M. Brown, R. Sundararaman, P. Narang, W. A. Goddard, III, and H. A. Atwater, Ab initio phonon coupling and optical response of hot electrons in plasmonic metals, Phys. Rev. B **94**, 075120 (2016).

[43] C. Jian, X. Ma, J. Zhang, and X. Yong, Strained $MoSi_2N_4$ monolayers with excellent solar energy absorption and carrier transport properties, J. Phys. Chem. C **125**, 15185 (2021).

[44] M. Bernardi, D. Vigil-Fowler, C. S. Ong, J. B. Neaton, and S. G. Louie, Ab initio study of hot electrons in GaAs, Proc. Natl. Acad. Sci. **112**, 5291 (2015).

[45] C. Jian, J. Zhang, and X. Ma, Cu-Ag alloy for engineering properties and applications based on the LSPR of metal nanoparticles, RSC Adv. **10**, 13277 (2020).

[46] X. Ma, H. Sun, Y. Wang, X. Wu, and J. Zhang, Electronic and optical properties of strained noble metals: Implications for applications based on LSPR, Nano Energy **53**, 932 (2018).

[47] T. Christensen, *From Classical to Quantum Plasmonics in Three and Two Dimensions* (Springer Theses, New York, 2017).

[48] T. Stauber, Plasmonics in Dirac systems from Graphene to topological insulators, J. Phys. Condens. Matter **26**, 123201 (2014).

[49] S. A. Maier, *Plasmonics Fundamentals and Applications* (Springer, Berlin, New York, 2007).

[50] A. Catellani and A. Calzolari, Plasmonic properties of refractory titanium nitride, Phys. Rev. B **95**, 115145 (2017).

[51] P. Patsalas, N. Kalfagiannis, and S. Kassavetis, Optical properties and plasmonic performance of titanium nitride, Materials **8**, 3128 (2015).

[52] C. Lian, S. Q. Hu, J. Zhang, C. Cheng, Z. Yuan, S. Gao, and S. Meng, Integrated Plasmonics: Broadband Dirac Plasmons in Borophene, Phys. Rev. Lett. **125**, 116802 (2020).

[53] P. M. Echenique, M. P. J., E. V. Chulkov, and A. Rubio, Theory of inelastic lifetimes of low-energy electrons in metals, Chem. Phy. **251**, 1 (2000).